A swarm of dusty objects in orbit around the central star of planetary nebula WeSb 1

Jan Budaj ®[1] ✉, Klaus Bernhard ®[2], David Jones ®[3,4,5] & James Munday[6]

Exoplanets and smaller bodies have been detected orbiting different kind of stars. However, we do not know of any such objects in planetary nebulae, the short-lived stage of stellar evolution between the asymptotic giant branch and white dwarf phases. The planetary activity (destruction and formation) may be accompanied by dust clouds. Hence, we searched for dust occultation events in planetary nebulae using archival photometric data. We show that the central star of PN WeSb 1 features numerous dimming events with typical durations of a few days to weeks that are up to 3 mag deep. This variability is mainly stochastic with an indication of a 400 d period. The occultations are almost grey, indicating dust grains larger than about 0.1 μm. Based on our follow-up observations, we argue that the central star is a wide binary and that these events are most probably caused by debris from disintegrated small rocky bodies that escaped from the former asymptotic giant branch star to find safe harbour around the companion star. The latter star dominates the optical spectrum enabling us to see the eclipses. This means that planetary systems are present and undergo violent evolution during the planetary nebula stage.

It is now clear that stars in our Galaxy are not alone but, rather, are orbited by any number of planets, asteroids or smaller bodies. In fact, the average number of planets around Sun-like stars is larger than one, and the fraction of such stars with at least one planet is between 45% and 100%[1–3]. Collisions between such objects are often associated with dusty debris disks that are observed in about 25% of stars[4,5]. During the asymptotic giant branch (AGB) phase of stellar evolution, stars expand and lose a substantial fraction of their mass. The AGB star engulfs bodies on closer orbits, as its radius increases to an astronomical unit or more. Owing to the heavy mass loss from the star, the orbits of bodies that are further away may become unstable[6,7]. As these AGB stars evolve to become white dwarfs (WDs), some of the bodies in unstable orbits can get very close to the WD, where they are tidally disrupted into dusty debris. This dust emits infrared (IR) radiation and accretes onto the WD, contaminating its surface with heavy elements. Such a scenario has been proposed to explain the metals in the atmospheres of WDs and their IR excesses[8,9]. Over the last decade, exoplanets, exoasteroids and associated debris have been found in close orbits around WDs[10–16],

which confirms the aforementioned scenario (see also a recent review in ref. 17). However, this process has not been observed between the AGB and WD phases.

Planetary nebulae represent a short-lived phase of stellar evolution between the AGB and WD phases. Many planetary nebulae are probably the product of a common envelope (CE) evolution, during which a companion star is engulfed by the AGB star, resulting in the rapid ejection of its envelope[18]. The ejected material has high metallicity and tends to be focused in the orbital plane to create a dusty disk[19], sometimes with a clumpy spiral pattern[20,21]. Such structures may have favourable conditions for the formation of a second generation of planets or may feed a surviving first generation of planets with new material[22–27]. Indeed, exoplanets have recently been detected around post-CE binaries (for example, refs. 28–30). However, it is still not clear whether these planets survived the CE or are second-generation planets[31]. Apart from that, more than 20% of hot WDs, which are central stars of planetary nebula, show an IR excess[32]. It has been argued that for the Helix nebula, the IR excess may be due to dust originating

[1]Astronomical Institute, Slovak Academy of Sciences, Tatranská Lomnica, Slovak Republic. [2]Bundesdeutsche Arbeitsgemeinschaft für Veränderliche Sterne e.V. (BAV), Berlin, Germany. [3]Instituto de Astrofísica de Canarias, La Laguna, Spain. [4]Departamento de Astrofísica, Universidad de La Laguna, La Laguna, Spain. [5]Nordic Optical Telescope, Breña Baja, Spain. [6]Department of Physics, University of Warwick, Coventry, UK. ✉e-mail: budaj@ta3.sk
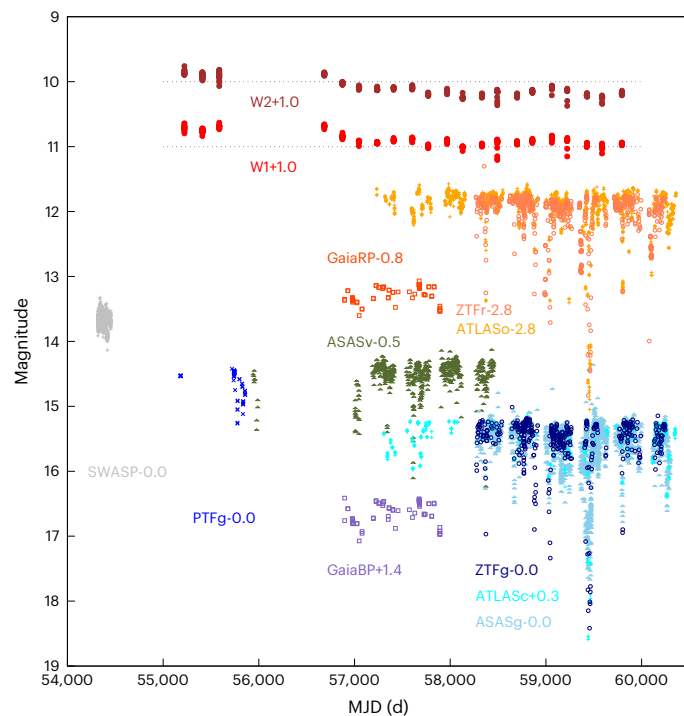
Fig. 1 | Long-term variability of planetary nebula WeSb 1 at various filters. WISE/NEOWISE W2 (brown full circles) and W1 (red full circles); ASAS-SN V (green triangles) and g (sky-blue triangles); ATLAS c (cyan plus signs) and o (orange plus signs); ZTF r (open orange circles) and g (open navy-blue circles); Gaia BP (purple squares) and RP (red squares); PTF g (blue crosses); SuperWASP (grey plus symbols). Observations in some filters are offset for clarity. The offset in magnitudes is indicated in the labels. Dotted lines along the W1 and W2 filters are used to guide the eye.

from a remote cloud of comets[33]. Dust clouds associated with both the destruction of old planets or the formation of new planets may eclipse the central stars of planetary nebulae.

All this motivated us to search for dust occultation events in planetary nebulae. We assessed about 1,935 planetary nebulae from the catalogue of ref. [34] and found one planetary nebula with clear occultations (WeSb 1), which is the subject of this paper. Apart from that, we searched the literature and found six planetary nebulae that show obscuration events due to dust, as summarized in the Supplementary Information (Appendix A). None of these had previously been thought to be associated with planets or smaller bodies. However, the behaviour of one of them (PHR 1806-2652)[35] may resemble that of WeSb 1, and it would be interesting to reanalyse this object in the light of our results. Considering both objects, the rarity of this phenomenon among planetary nebulae is of the order of 1:10[3].

An overview of the basic properties of PN WeSb 1 and its central star (Gaia DR3 423384961080344960) can be found in 'WeSb 1 and its central star'. All further mentions of 'the star' will refer to the central star of the nebula. Note that, in general, it may not be a single star but could be, for example, a binary star, in which case the central star of the planetary nebula is the post-AGB component.

Results

Long-term variability from wide-field surveys

We compiled the photometric observations of this star using several filters from several sources: the All Sky Automated Survey for Super-Novae (ASAS-SN)[36,37], Palomar Transient Factory (PTF)[38], SuperWASP[39], Gaia[40,41], the Asteroid Terrestrial-impact Last Alert System (ATLAS) project[42,43], Zwicky Transient Facility (ZTF)[44] and Wide-field Infrared Survey Explorer (WISE)[45,46].
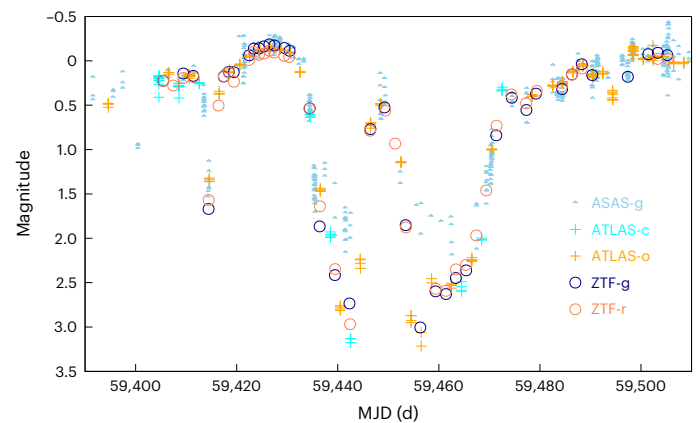
Fig. 2 | Deep eclipse event in July to October 2021. ASAS-SN g (sky-blue triangles); ATLAS c (cyan plus signs) and o (orange plus signs); ZTF r (open orange circles) and g (open navy-blue circles). Observations in the filters were offset by their median value.

The observations mentioned above are described in 'Archival photometric data and properties of eclipses' and are plotted in Fig. 1. Overall, they show a stable brightness (plateau level) that is pierced by numerous dimming episodes, which we will refer to as dips, obscurations or eclipses. They are unlikely to have been caused by 'classical' eclipses due to large, spherical and non-transparent bodies such as stars. Rather, they are the result of dust obscuration or condensation. An extreme event occurred during MJD 59,400–59,500, which had several dips deeper than 1.5 mag. We did not even see the floor of this event in the ASAS-SN data, as the ASAS-SN telescopes are very small and cannot go much deeper that 17 mag. Fortunately, this event was recorded in both ZTF r and g. It is displayed in a separate Fig. 2. The duration of the event was about 3 months, spanning July to October 2021. During this period, the brightness of the star dropped on several occasions, with two such dips being almost 3 mag deep. The brightness of the star in the near-IR region was either constant or decreasing by about 0.3 mag. Occasionally, it briefly dropped by up to 0.2 mag. Unfortunately, none of the IR observations coincide with any of the principal dips observed in the optical region.

Supplementary Fig. 1 is a closer look at several other events in the optical region. One can see some double or triple dips. A more detailed analysis of numerous individual transit features can be found in 'Archival photometric data and properties of eclipses'. There is no obvious periodicity but several events are separated by roughly 400 days. This weak periodicity was confirmed by a period search of the optical data. The resulting Lomb–Scargle periodogram is shown in Supplementary Fig. 2. The two most pronounced peaks are at 390 and 260 days and may be in a 2:3 resonance ('Archival photometric data and properties of eclipses'). Analysing the SuperWASP data alone led to the identification of another shorter periodicity of 14 days.

In addition, the Transiting Exoplanet Survey Satellite (TESS)[47] observed this field in 2019 and 2022. These data show an interesting chain of at least five relatively fast symmetric events in sector 58 and almost constant brightness (within 1%) during sector 18. These are described in 'TESS photometry'.

Spectral energy distribution

The overall spectral energy distribution (SED) contains important information on the nature of the star. A detailed analysis of the SED can be found in 'Spectral energy distribution' in Methods and in Fig. 3. The SED of WeSb 1 can be split into three components with the following characteristic temperatures and radii: $T_1 = 5,890 \pm 90\,\text{K}, R_1 = 4.1 \pm 0.2\,R_\odot$, $T_2 = 1,360 \pm 70\,\text{K}, R_2 = 74 \pm 8\,R_\odot$, and $T_3 = 280 \pm 40\,\text{K}, R_3 = 910 \pm 200\,R_\odot$, respectively. The corresponding luminosities are about 18, 17
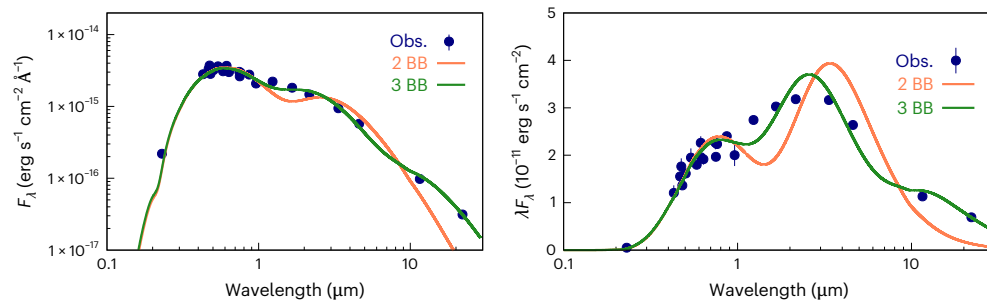
Fig. 3 | SED of WeSb 1. Left, the representation in log–log scale (flux F vs. wavelength λ) clearly indicates an IR excess. Right, the λF_λ representation demonstrates that most of the energy is, in fact, radiated at IR wavelengths. Observations are depicted by the blue circles as mean values with standard deviation error bars. The orange and green lines denote, respectively, a simple two-black-body fit and a three-black-body fit to the data. 2 BB, two black bodies; 3 BB, three black bodies; Obs., observed data.

and 5 $L_\odot$, respectively. The first SED component dominates the optical region where the eclipses are observed. Its parameters indicate a G-type subgiant star, which is confirmed in 'Spectroscopy' (Methods) with the detection of its absorption lines. It does not correspond to a typical central star of a planetary nebula but rather a companion star orbited by dust clouds ('Spectral energy distribution' in Methods). Note that the eclipsing bodies must be at least 8 $R_\odot$ in size to cause such deep eclipses. The temperature of the second component is close to the condensation temperature of refractory dust species and probably represents the radiation from the inner edge of a dust disk. The third SED component probably represents more extended and cooler dust regions emitting in the vicinity of silicate bands at 10–20 μm. Apart from these components, there is probably an undetected hot central star. The luminosities of the dust components are much lower than that of a typical planetary nebula. This is most probably because the planetary nebula is very old, so that the central star of the planetary nebula is already below the knee in the Hertzsprung–Russell diagram on a WD cooling track[48], or because the central star is hidden in an edge-on disk ('Spectral energy distribution' in Methods) or because the dust is not associated with the central star of the planetary nebula but with a secondary star.

Follow-up observations

We obtained further images, spectroscopy and photometry of the central star. Technical details are described in 'Imaging', 'Spectroscopy', 'Photometry' and 'TESS photometry' in Methods, and a summary of our observations is given in Supplementary Table 4.

Narrowband imaging. The nebula was clearly detected with both the Hα and [O III] λ5007 filters, as shown in Supplementary Fig. 3. These data were combined to give the synthetic colour image in Fig. 4. The nebula appears to be roughly spherical and has a similar extent in both filters. This is consistent with the planetary nebula having not experienced a CE stage of binary-star evolution. On the other hand, the central star is slightly offset from its centre, a property often associated with central star binarity[49,50] or an interaction with the interstellar medium[51]. The latter hypothesis is supported by the nebula being significantly brighter on the northern side towards which the central star is displaced, as in Fig. 7(b) of ref. 51. The proper motion of the star, that of neighbouring stars, the offset direction of the star as well as the planetary nebula axis of symmetry are all roughly aligned, which may not be an accident. However, the proper motion of the star with respect to its neighbourhood does not point towards the brighter hemisphere. Thus, the shape of the planetary nebula, its interaction with the surrounding interstellar medium and the offset of the star remain open questions.

Assuming an angular radius, distance and a typical constant expansion velocity of 92", 3,670 pc and 20 km s^{-1}, respectively, leads
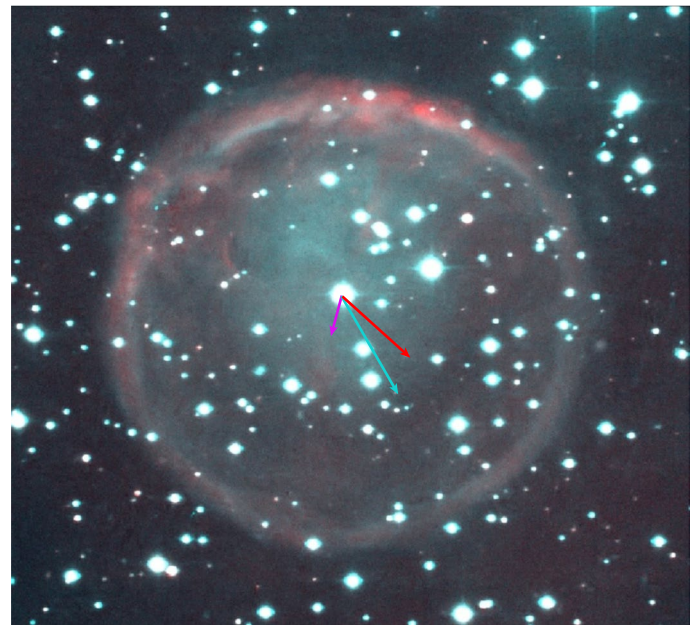

Fig. 4 | Synthetic colour image of WeSb 1. The data were obtained from the Hα filter (red) and the [O III] λ5007 filter (green and blue). The image measures 4' × 4'. North is up, and east is left. Blue, red and magenta arrows indicate the proper motion vectors of the star, the ISM and the star with respect to the ISM, respectively.

to a planetary nebula radius of about 1.65 pc and an approximate kinematical age of the nebula of about 80 kyr. This ranks WeSb 1 among the biggest planetary nebulae. For comparison, the oldest PN IPHASX J055226.2+323724 has a very similar parameters, with a radius of 1.6 pc and an age of 78 kyr (ref. 52). Even more similar, EGB 6 is a large (2 pc), nearly spherical planetary nebula that also has an unresolved high-density core and an IR excess[53].

Spectroscopy. Our spectroscopic observations are described in more detail in 'Spectroscopy' (Methods). The overall observed (not corrected for reddening) and flux-calibrated spectrum is shown in Fig. 5. There are emission lines for the following ions: H I, He I–II, [N II], [O III], [Ne III], [Ar III] and [Ar V]. The identification of the last ion is questionable. We did not detect any carbon lines, which indicates that the environment is not rich in carbon. Hα is the strongest line in the spectrum, followed by [O III] λ5007. The strength of these lines and that the star is well above the background in our narrowband Hα and [O III] λ5007 images indicate that the planetary nebula itself does not affect these emission lines significantly and that the latter originate from an unresolved
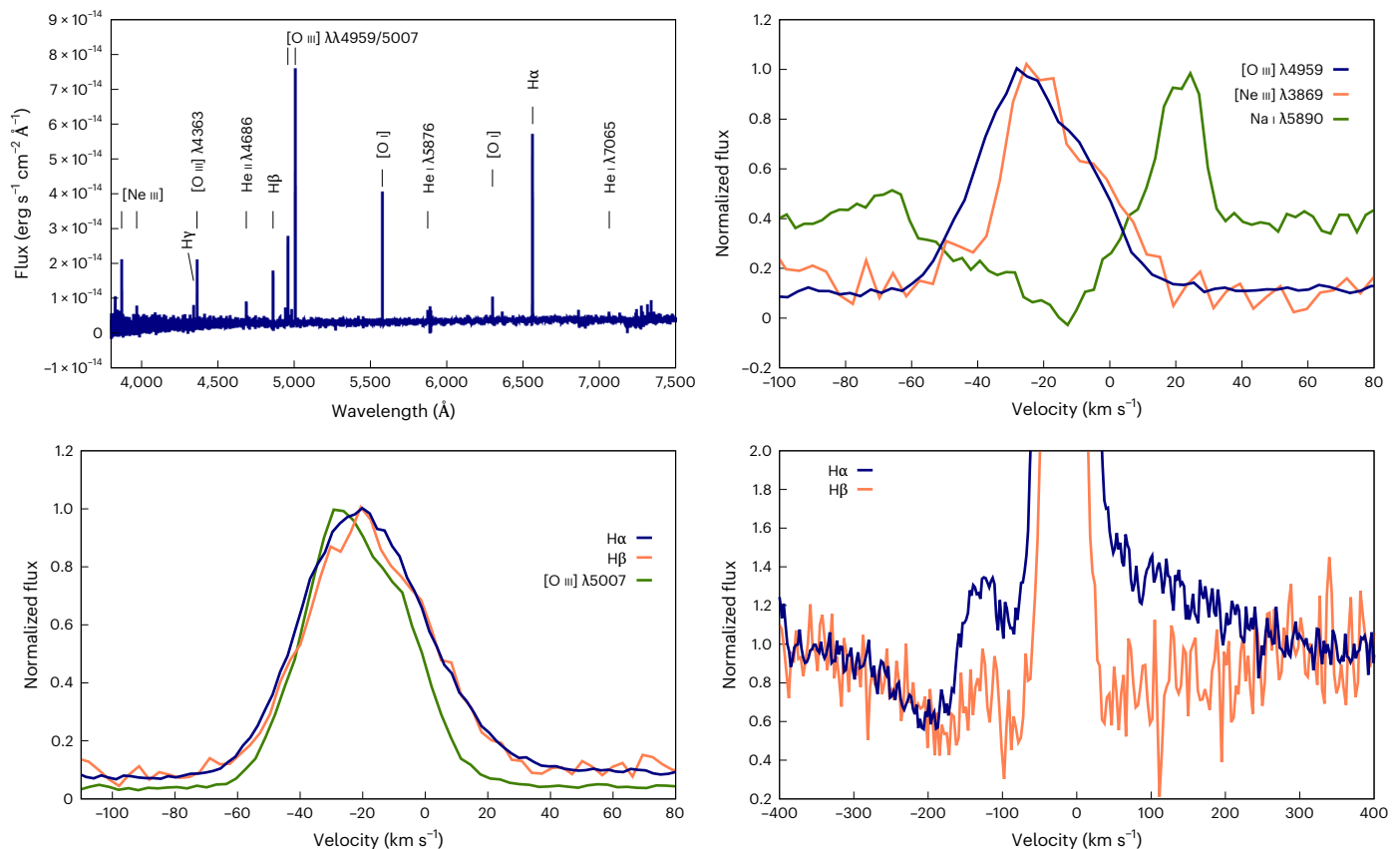
Fig. 5 | Spectra of WeSb 1. Top left, overall flux-calibrated spectrum of WeSb 1. Top right, the [Ne III] and [O III] line profiles are similar. Na I has an absorption at the same wavelength. Bottom left, Balmer line profiles also resemble the [O III] line profiles. Bottom right, Balmer lines show P Cyg line profiles with two absorption features in the blue wing.

nebula close to the central star of the planetary nebula ('Spectroscopy' in Methods). Assuming that this unresolved nebula is photoionized by the central star of the planetary nebula, then, using different methods, there is a very broad range of possible temperatures of the central star from 40 to 150 kK ('Spectroscopy' in Methods). The He II lines are stronger than the He I lines and are significantly shifted to the red. This shift may be variable and needs to be investigated in future observations. Apart from that, we observe strong terrestrial emission lines of [O I] at λ5577, λ6300 and λ6364 Å and Na I at λ5890 and λ5896 Å.

All emission lines have a similar single-peak profile with a typical full-width at half-maximum (FWHM) of about 40 km s⁻¹. The radial velocities and fluxes in the spectral lines are summarized in Supplementary Table 1. Most emission lines have consistent heliocentric radial velocities of about −20.2 km s⁻¹ with [Ne III] lines having slightly lower velocities than the [O III] lines. The Na I lines have an absorption feature at the same velocities. This is also illustrated in Fig. 5. This indicates that all these lines originate from co-moving regions within 3″ from the star and not from the planetary nebula itself. The Hα and Hβ lines have P Cyg type profiles with two absorption features: a blue absorption at about −90 km s⁻¹ and a far-blue absorption at about −200 km s⁻¹. Red emission in Hα extends up to 250 km s⁻¹ (Fig. 5). The [N II] λ5755 line also has a similar blue absorption component. One might speculate that these absorption components correspond to two different envelopes expanding at different velocities or to a stellar or disk wind[54]. These absorption components may also be variable. The [O III] λ5007/Hβ line ratio of about 4 is too low, whereas [O III] λ4363/ Hγ of about 2 is too high for a typical planetary nebula. These ratios may have increased over the period covered by our observations. It is important to note that the emission lines contribute very little to the total flux in the broadband filters. In particular, the line to continuum

flux ratios for the ZTF g, ZTF r, ATLAS c and ATLAS o filters are 0.021, 0.012, 0.013 and 0.007, respectively ('Spectroscopy' in Methods).

We were able to detect also the absorption lines corresponding to the spectrum of a G-subgiant star with an indication of Ba enhancement, which is in agreement with the first SED component being a companion star ('Spectroscopy' in Methods).

Photometry. We observed the central star of WeSb 1 for about 5 h in the B and R filters with the 1.3 m telescope at Skalnaté Pleso Observatory. We aimed to detect pulsations or any variability on timescales of minutes or hours that were not covered by long-term monitoring and archival data. The resulting differential photometry is shown in Supplementary Fig. 4. The star was almost constant in the R filter (within 0.01 mag), whereas in the B filter, there was weak variability at the level of about 0.01 mag.

Interpretation and discussion
Such numerous, deep and irregular eclipses cannot be caused by stars. The eclipsing objects must be large and bigger than the main source of visible light, which has a size of at least 8 $R_\odot$ ('Spectral energy distribution' in Methods). Matter in the form of dust has a much higher opacity than gas, and the presence of dust is indicated by the IR excess. Therefore, it seems probable that the photometric variability is due to dust clouds. The opacity of dust depends on wavelength and the grain properties, such as their particle size and chemical composition. Consequently, multi-wavelength observations of the eclipses may constrain these dust properties. To this end, we searched for colour-dependence in the dimming events using observations with the ZTF r, ZTF g, ATLAS c and ATLAS o filters ('Properties of dust grains'). The main result being that the dust grains are composed of relatively large particles, larger

than 0.1 μm, with the exception of smaller eclipses that might also be caused by ~0.06 μm carbon or iron grains. Subsequently, further questions arise about the nature of such dust clouds.

A detailed discussion of several possible scenarios, open questions and suggestions for future work is given in the Supplementary Information (Appendix B). These include three less probable scenarios: (A) R Coronae Borealis-like dust condensation, (B) a symbiotic star and (C) an optical double star. The most probable are scenarios (D) and (E). Scenario (D) presumes a circular, clumpy, edge-on Keplerian dust disk around the G subgiant or a circumbinary disk (the latter being less probable). The disk causes an analogue of UX Orionis-like variability. Scenario (E) assumes the existence of numerous smaller bodies, such as exoasteroids or exocomets, on similar, long-period and eccentric orbits around the G subgiant or around the binary (the latter being less probable). The bodies may have originated from a disintegration of a common progenitor and are surrounded by debris dust clouds causing sequences of eclipse events.

The properties of our planetary nebula resemble those of EGB 6, which is an ancient, large planetary nebula (2 pc), with a nearly spherical shape, a high-density nebula, IR excess and a distant companion[53]. We propose the following hypothesis, which may explain both WeSb 1 and EGB 6. Initially, an AGB star is orbited by numerous small rocky bodies and another, more distant, companion star (a G subgiant). The AGB star loses most of its mass, which destabilizes the orbits of the smaller bodies. In this binary, with the Roche lobe of the AGB star shrinking and the lobe of the G subgiant expanding, a fraction of the bodies and dust material may wander from the former into the latter Roche lobe and become focused into the orbital plane. As the AGB star turns into a hot central star of the planetary nebula, it becomes very hostile for small bodies and dust that are close to it. However, 'our' bodies can find a safe harbour around the more distant G subgiant, where they collide with each other or with native population of small bodies around the G subgiant to produce a debris disk and dust clouds. As the G subgiant shines in the optical region, we can observe these dust clouds eclipsing the star.

Conclusion

We have discovered a planetary nebula whose central star is being eclipsed by numerous dust clouds. The planetary nebula itself was detected with the Hα and [O III] λ5007 filters. It has an apparently spherical shape with the central star slightly offset to the north. At the Gaia distance of the central source, WeSb 1 would be one of the oldest and largest planetary nebulae known. The non-background-subtracted spectrum of the star also shows strong Hα and [O III] λ5007 emission lines, probably originating from an unresolved nebula close to the star. The SED of the star features a strong IR excess, which also indicates the presence of relatively hot dust. We argue that the central star is a binary and that the dust clouds are associated with a debris disk or disintegrated smaller bodies orbiting and eclipsing the secondary star, which shines in the visual domain. This may be the first indication of small dusty bodies in the close vicinity of a central star of the planetary nebula. The object represents a missing link in the evolution of planetary systems between the AGB and WD stages of stellar evolution.

Methods
Spectral energy distribution
The SED of WeSb 1 was constructed using the VOSA tool[55] and considering only broadband photometry. This SED is shown in the left panel of Fig. 3. As demonstrated in Fig. 1, the star may experience brightness fluctuations by about 3 mag, which could significantly impact the SED, as the different wavelengths observed are obtained at different phases of its variability. However, most of the time, the variability is less than 0.3 mag, probably mitigating this issue. Similarly, as outlined in 'Spectroscopy' ('Results'), the integrated spectrum of the star and surrounding nebulosity have strong emission lines. However, these lines do not affect the SED significantly.

The observations indicate that the flux peaks in the optical region and that there is a significant IR excess. The scatter is larger than the error bars, which is due to the above-mentioned variability of the source. For this reason, it was difficult to estimate the interstellar extinction from the SED and justify approximating the SED with stellar atmosphere models that feature absorption lines. So, we adopted a fixed distance of 3,340 pc from ref. 56 and a fixed extinction of $E(B - V) = 0.255$ obtained using three-dimensional extinction maps from ref. 57, and we assumed a canonical value of $R_V = 3.1$, which translates into $A_V = 0.80$ mag. Then, we fitted the full SED using an adapted version of the code presented in ref. 58, which uses a Markov chain Monte Carlo algorithm with the Python package emcee[59] to maximize the likelihood between all survey photometry of WeSb 1 and a multi-component black-body model, thus integrating the model SED over the transmission function of each source. The free parameters were the temperature and radii of each component, all with flat priors. The reddening was taken into account using the recent extinction curves of ref. 60. The reddening was applied to the black-body models (not to the observations), which is why the curves in Fig. 3 feature a bump at 0.2 μm. An initial burn-in phase was performed and discarded once all chains had converged. We used 500 walkers, and 500 burn-in and post-burn-in iterations were performed, as the initial 500 iterations were easily sufficient for model convergence. Owing to the variability of the source, we ascribed a further uniform error to each point in quadrature to the observed error to ensure that the reduced χ^2 of all points equalled 1 (10.5%). First, a model with two black-body components was applied. The temperatures and radii of the two components were $T_1 = 5,810 \pm 100$ K, $R_1 = 4.3 \pm 0.2$ $R_\odot$ and $T_2 = 1,050 \pm 100$ K, $R_2 = 130 \pm 30$ $R_\odot$, respectively. The fit is shown in Fig. 3. We caution that although we used non-transparent spherical black bodies, the real objects may be very different; they do not have to be spherical stars, and they do not even have to be optically thick.

The log–log representation of the SED shown in the left panel of Fig. 3 can be very misleading, which is why we also present the λF_λ versus $\log \lambda$ representation in the panel on the right. It demonstrates that, although the optical region is important, the star radiates most of the energy at IR wavelengths within the 1–6 μm interval. This picture also indicates that a simple two-component black-body model does not fit the IR radiation very well.

The situation improved when we added a third black body to the solution, which led to the following parameters: $T_1 = 5,890 \pm 90$ K, $R_1 = 4.1 \pm 0.2$ $R_\odot$, $T_2 = 1,360 \pm 70$ K, $R_2 = 74 \pm 8$ $R_\odot$, and $T_3 = 280 \pm 40$ K, $R_3 = 910 \pm 200$ $R_\odot$, respectively. An F-test revealed that the addition of the third component was justified and significant at the 6σ level. The posterior probability distribution is shown in Supplementary Fig. 5. The errors assume that the distance and the extinction are fixed. The corresponding luminosities of the components are 18, 17 and 5 $L_\odot$, respectively. This fit is also shown in Fig. 3. The parameters of the first black-body component do not change much. Its temperature is in agreement with that derived from Gaia (Supplementary Table 2) and principally represents the radiation in the optical regime. Its radius is significantly larger than the radius of a star on the main sequence with the same temperature. Rather, it corresponds to a G-type subgiant star. It is too cold to be the central star of a planetary nebula and is probably a secondary star. This was confirmed in 'Spectroscopy' (Methods) by the detection of absorption lines associated with this component. Its size, the absence of a reflection effect and ellipsoidal variability in the light curves, and the projected spherical shape of the planetary nebula indicate that it is not a close post-CE binary. Hence, it is probably on a long-period orbit but might have been contaminated with some material from the former AGB star, which is indicated by the enhanced Ba abundance ('Spectroscopy' in Methods). Assuming the evolutionary models of ref. 61, its luminosity and temperature would correspond to a star with a mass and age of 1.8 $M_\odot$ and 1.6 Gyr, respectively. The second body is slightly hotter and smaller than when assuming two

black bodies. Note that this temperature is close to the condensation temperature of refractory dust species (1,500 K) and dominates the radiation in the near-IR region. Its radius suggests a giant star, but it most probably represents an inner dust disk. The third body is very cool and represents an enhanced IR radiation from the object in the vicinity of silicate bands at 10–20 μm. Hence, it too is made of dust. It is not known whether the IR excess is associated with the central star of the planetary nebula, the G-subgiant star or both. Clearly, there is still room for improvement in the fit, and a more sophisticated model must be used to properly account for the observed IR excess.

To constrain the dust mass, we calculated the amount of IR dust emission emitted by a dust cloud that is optically thin. We assumed particles made of carbon, iron or iron-rich silicates, with sizes ranging from 1 to 30 μm, dust opacities from ref. [62], and with temperatures indicated by our three-black-body fit. In the optically thin limit, the IR emission is not sensitive to the geometry of the dust cloud. This allowed us to place a lower limit on the amount of dust causing the IR excess to $10^{-9}\,M_\odot$ or $10^{-3}\,M_\oplus$. Hence, this dust may theoretically originate from a collision of Moon-sized bodies or from a disintegration of an equivalently larger number of smaller bodies.

Apart from these SED components, there is probably a much hotter but more compact star in the centre of the planetary nebula. We did not see it in this SED, but it is indicated by spectroscopy and the appearance of He II and other lines of highly ionized species. Adding a simple, unobscured, hot component to the model would require two more free parameters (its temperature and radius), but it would be poorly constrained by the observations, as it may affect only one point (near-ultraviolet (NUV) point detected by the Galaxy Evolution Explorer (GALEX)). Unfortunately, the temperature from spectroscopy gives a very broad range of possible values for this component (from 40 to 150 kK, see 'Spectroscopy' in Methods). Thus, we did not include this hot star in our SED modelling. However, assuming that the lowest possible radius of the hot star is the typical radius of a WD ($0.01\,R_\odot$) would give us the highest possible temperature and luminosity that are still compatible with the NUV GALEX point. These are 130 kK and $26\,L_\odot$, respectively. However, the luminosity of central star of the planetary nebula might be higher if it were embedded in a disk. We also verified that adding such a hot SED component would affect only the NUV point and would not change the parameters of our three SED components significantly.

Evolutionary models may give further insights into the properties of the central star and the evolutionary status of the system. Assuming a very uncertain kinematical age of the system of 80 kyr ('Narrowband imaging') and using the solar metallicity and evolutionary models of ref. [48] for the initial stellar masses of 1–4 $M_\odot$, the temperature of the star would be about 100 kK, its luminosity about 20–100 $L_\odot$ and radius about 0.013–0.04 $R_\odot$. This would mean that, in the Hertzsprung–Russell diagram, the star is already below 'the knee' on a cooling track towards the WDs. Assuming the highest luminosity of a central star of a planetary nebula of 100 $L_\odot$ would put a lower limit on the fractional luminosity of the dusty disk relative to both stars. It has to be larger than about 0.17, which is significantly more than what is typical for debris disks around main sequence stars (<0.8%)[5]. This indicates that our debris disk is not the same as debris disks around main sequence stars. Its IR excess is rather comparable to the IR excess found by ref. [32] around some WDs with dusty disks that are central stars of planetary nebulae.

Properties of the dust grains

The properties of the dust grain can be derived from multi-wavelength observations. ZTF g, ZTF r and ATLAS c, ATLAS o could be used for this. The problem is that the fluxes in these filters are contaminated by emission lines. These lines probably originate from an unresolved nebula close to the star, but such a nebula is probably too big to be eclipsed by our dust clouds. The contamination is very small, only about 0.022,

0.013, 0.014 and 0.008 mag in the ZTF g, ZTF r, ATLAS c and ATLAS o filters, respectively ('Spectroscopy' in 'Results'). Nevertheless, it can be important during deep eclipses. Thus, for the purpose of this section, we subtract the contribution of the emission lines from these filters.

The other problem is that our star is extremely variable, which means that such multi-wavelength observations need to be simultaneous. However, they were obtained at different moments. Note that ZTF r and ATLAS o filters are very similar and contain more data than the other filters. Thus, we merged the observations in these two filters into one sample, which we will refer to as 'r-red'. This enabled us to get a better time coverage in the red filter. Then we interpolated the values in the red filter to the same time as observations by ZTF g and ATLAS c. The brightness of the star in ZTF g and ATLAS c as a function of the values for the red filter is shown in the left panel of Supplementary Fig. 6. As one can see, there is a very tight linear correlation between the two. We fitted a straight line to the data in the form:

$$\text{ZTF}g = a_1 + b_1 \times r \qquad \text{ATLAS}c = a_2 + b_2 \times r. \qquad (1)$$

The coefficient values are listed in Supplementary Table 3. The slopes ($b_1 = 1.092$ and $b_2 = 1.060$) are only slightly above one.

However, it looks like the shallow dips have a slightly steeper slope than the deeper ones. This is better seen in the right panel of Supplementary Fig. 6. We plotted the red filter as a function of the colour indices $g - r$ and $c - r$. Unfortunately, the $c - r$ index has a huge spread of about 1 mag and very poor coverage for the deep eclipses, which is why we do not use it in the following analysis. The slope or reddening vector for eclipses deeper than $r = 15.3$ mag is almost vertical, which means that these eclipses are almost grey (not depending on the wavelength). Thus, we fitted separate slope vectors for shallow and deep eclipses. These parameters are also listed in Supplementary Table 3, and the fits are displayed in Supplementary Fig. 6 by straight lines. For comparison, we plot also the one-to-one dependence in the figure.

If the eclipsing objects (dust grains) are much larger than the wavelength of the light, then this would imply a geometrical optics regime and 'grey' eclipses. This is the case for very large dust grains and even transiting exoplanets (without the atmosphere). On the other hand, if the transiting objects are much smaller than the corresponding wavelength, then a Rayleigh scattering regime would apply. This regime is strongly dependent on the wavelength (as λ^{-4}) and eclipses at the shorter wavelength would be significantly deeper. The value of the slope $b_1 = 1.092 \pm 0.007$ indicates that the eclipses are almost grey, and that we are just on the onset towards the first regime.

Note that the attenuation of light expressed in magnitudes Δm_λ is proportional to the optical depth τ_λ. Namely,

$$\Delta m_\lambda = 1.086\tau_\lambda. \qquad (2)$$

The optical depth is proportional to the opacities κ_λ and geometrical depth. Consequently, the ratio of Δ magnitudes in different filters (that is the slope b_1) is proportional to the ratio of the dust opacities at the corresponding wavelengths:

$$b_1 \equiv \frac{\Delta m_{\lambda_1}}{\Delta m_{\lambda_2}} \approx \frac{\kappa_{\lambda_1}}{\kappa_{\lambda_2}}. \qquad (3)$$

Hence, our observations of the slope b_1 can be directly compared with calculations of dust opacity ratios. The opacities of grains with different chemical compositions and different modal particle sizes were taken from the tables of ref. [62]. We considered mainly refractory grains but included also volatile ammonia and water ices, as the dust might originate from the larger debris on eccentric orbits and be freshly produced from continuing collisions. The opacities correspond to the effective wavelengths of ZTF g and red filters, which are about $\lambda_1 = 0.475$ and $\lambda_2 = 0.650$ μm, respectively. These opacities

assume homogeneous spherical dust grains with a relatively narrow Deirmendjian particle size distribution[63]. The observed and theoretical opacity ratios for different modal grain sizes and chemical compositions are compared in Supplementary Fig. 7. One can clearly see the two regimes: the Rayleigh regime with the steep opacity ratio for small particles and the geometrical optics regime with the flat opacity ratio for large particles. Our observations of the slopes for shallow and deep eclipses are also plotted.

The deep eclipses are almost grey, and we could put only a lower limit for the sizes of particles made from different species. Pure iron or carbon particles have to be larger than about 0.1 µm, silicates or alumina (corundum) 0.2 µm, ammonia 0.3 µm, and water ice larger than 0.4 µm in size. Shallow eclipses are best reproduced with 0.06 µm iron/carbon particles, 0.1–0.2 µm silicate/alumina particles, 0.2 µm ammonia or 0.3 µm water ice grains.

These are relatively large particles, larger than in the interstellar medium. In reality, it is very probable that there is a mixture of even larger particles with somewhat smaller particles. In fact, such almost grey eclipses resemble grey transits caused by disintegrating exoasteroids orbiting the white dwarf WD1145+017 (refs. 64–68). These transits become shallower in the blue or UV region[69,70], which is partially due to forward scattering of dust[71]. It is possible that deeper transits in our object are also affected by this effect. Observations at a broader interval of wavelengths would put further constraints on the properties of the dust grains.

WeSb 1 and its central star

PN WeSb 1 (PN G124.3 − 07.7) was discovered by Weinberger and Sabbadin, who were performing interference filter photography for Hα and [O III] λ5007 lines[72]. The nebula was detected on only the Hα plate and not on the [O III] plate. Nevertheless, the nebula had already been seen in Palomar Observatory Sky Survey prints but this detection was not unequivocal. It had the shape of a half-ring with a diameter of 155″. The same authors estimated its distance to be 1,500 pc.

The authors of ref. 73 took deeper images with a 2.1 m telescope of the Hα, [N II] λ6584, [S II] λ6719 and [O III] λ4363 lines. The planetary nebula was not detected in [S II] images, whereas the other bands showed a complete rounded ring-like structure with a diameter of about 3′. Those authors argued that the circular profile of WeSb 1 is a projection of a spherical shell. Their [O III] photograph showed two blue stars in the centre, indicating that one was probably the planetary nebula nucleus.

The nebula is in the constellation Cassiopeia. A finding chart from ref. 74 had already identified a star in the centre as a probable nucleus, Gaia DR3 423384961080344960. The same star was detected by GALEX in the NUV as well as in 2MASS in the near-IR maps. Images at a few selected wavelengths are shown in Supplementary Fig. 8. In the IR region (WISE W1–W4), the star dominates the field of view, especially at the longest wavelengths. In the W3 and W4 filters, it is the brightest object in a 12′ × 12′ field. The nebula itself is seen in the red-optical region as a ring with a diameter of about 3′. The catalogue of ref. 75 gives a planetary nebula radius and distance of 92.50″ and 3,510 pc, respectively. The HASH database classifies WeSb 1 as a probable planetary nebula[76].

The basic properties of the star were taken from Gaia Data Release 3 (DR3)[40,41] and are summarized in Supplementary Table 2. To estimate the dust extinction towards the star, we consulted three-dimensional dust extinction maps from ref. 57. The extinction at this distance and in this direction is significant and amounts to $A(g) = 0.92$ mag. These results are also listed in Supplementary Table 2. Gaia found no other sources within ~10″ of Gaia DR3 423384961080344960. All sources within 20″ have very similar parallaxes (~0.2 mas). Roughly 30″ to the north and 30″ to the south there are stars with significantly larger parallaxes, corresponding to distances of 1 kpc or less. Thus, there is no evidence for a potential central star hidden so close to

Gaia DR3 423384961080344960 that is unresolved from the ground but which would place the nebula at a closer distance consistent with the statistical distance of 1.84 ± 0.35 kpc (ref. 77).

Archival photometric data and properties of the eclipses

The ASAS-SN Variable Stars Database[37] contains 11 years of observations with the g and V filters. In this database, the star is labelled as a variable, non-periodic, young stellar object (ASASSN-V J010054.10+550400.1)[78]. We removed the spurious data and points representing the upper limits from these observations. The PTF database[38] contains about 2 years of observations in the g filter. We downloaded the raw frames from the NASA/IPAC Infrared Science Archive and reduced them using MuniWin. The ATLAS project[42,43] observed this star for about 9 years with the c and o filters. We removed the points with errors larger than 0.05 mag. The star was observed also with SuperWASP-North[39]. These observations were performed with a very broadband filter (400–700 nm). We used data from only camera 5 (code = 145) and removed the points with errors larger than 0.1 mag. Gaia DR3 covers the period August 2014 to May 2017 in three filters G, BP and RP[40,41]. ZTF[44] has observed this star in two filters (ZTF g and ZTF r) for about 5 years. The WISE[45] and NEOWISE[46] databases contain 13 years of observations in the IR region (mainly the W1 and W2 filters).

These data are shown in Figs. 1 and 2. A few other eclipse events are shown in more detail in Supplementary Fig. 1. The SuperWASP data are the oldest and show a very mild variability of about 0.1 mag and a 1-day-long dip of about 0.3 mag at MJD 54,418. The PTF data exhibit a few days long and 0.7 mag deep dip at about MJD 55,776 followed by similar 0.2 mag deep event at MJD 55,836. Older ASAS-SN observations in the V filter feature several irregular drops in the brightness with durations ranging from 1 day up to a few weeks. The deepest dip occurred at MJD 57,613 and was 1.4 mag deep. The most recent observations with the ASAS-SN g filter indicate an enhanced activity with numerous dips lasting from a few days up to a month and deeper than 1 mag. An extreme event occurred during MJD 59,400–59,500, which was mentioned in 'Long-term variability from wide-field surveys'. Note that the dips are often clustered, occurring in pairs or in triples. Smaller dips (0.5 mag) are frequently followed immediately (within 10 days) by a deeper dip (1.5 mag) (for example, MJD 58,370 and 59,800) or vice versa (MJD 57,610 and 58,880). Apart from that, individual components of some double or triple dips are deeper than 1 mag (for example MJD 59,040 and 59,440). These features are impossible to explain by a dust cloud eclipsing (orbiting around) a binary or a triple star with components of comparable brightness. More probably, several clustered or structured dust clouds are eclipsing one main source of light at optical wavelengths, which is our first SED component in 'Spectral energy distribution' in Methods and which theoretically might orbit around another star of negligible brightness at optical wavelengths.

To characterize such events quantitatively, we fitted the individual eclipses deeper than about 0.3 mag with Gaussian functions of the form:

$$f(t) = c + b(t - t_0) + \sum_{i=1}^{n} a_i \exp\left[-\left(\frac{t - t_i}{d_i}\right)^2\right], \qquad (4)$$

where the summation runs through an optional number n of Gaussians and a_i, d_i and t_i are the amplitude, half-width at e^{-1} level and the centre of the ith Gaussian. The first two terms account for a possible linear trend. To increase the temporal sampling, we merged the observed data in all filters. This approach is justified for this purpose, as the eclipses are almost grey ('Properties of dust grains'). Thus, we obtained parameters for a few dozen events. Their full widths at the e^{-1} level and amplitudes are summarized in Supplementary Fig. 9. A typical duration for an event is from 1.5 to 20 days. Events shorter than 2 days are difficult to resolve owing to the cadence of the observations being similar. As one can see in the figure, there is no obvious correlation or anticorrelation between

eclipse depth and duration. In our case, the size of the dust clouds must be comparable to or greater than the diameter of the source of light in the optical region (~8 $R_\odot$) to cause such deep eclipses. Thus, the duration of such eclipses implies Keplerian velocities of about 7–90 km s⁻¹. Let us assume that these clouds are orbiting the G subgiant which has a mass of about 1.8 $M_\odot$ ('Spectral energy distribution' in Methods). Then, the above-mentioned velocities would result in star–cloud separations of about 0.2–40 au (or smaller if the clouds causing deep eclipses were bigger than the source of light).

A more realistic estimate of the distance of the clouds from the G subgiant can be obtained from the duration of the eclipse ingress or egress (whichever happens faster). This is like the gradient method used by ref. 79. From the duration of the ingress and the diameter of the source of light, one can calculate the velocity of the cloud by assuming that the cloud has a sharp edge and is bigger than the star. Then, assuming the mass of the star as above and the circular orbit, one can get the star to cloud distance. These distances are also illustrated in Supplementary Fig. 9. As one can see, they cover a broad interval of 0.3–40 au, confirming the above-mentioned estimates based on the eclipse duration. If the occulting dust cloud did not have a sharp edge, then the real star-crossing times would be shorter. Hence, these star–cloud separations should be viewed as an upper limits.

Note that in both methods (eclipse duration or ingress and egress), we assumed that the clouds orbit the G-subgiant star. They could also be circumbinary, that is orbiting a short-period binary comprising the central star of the planetary nebula and a G subgiant with masses of about 0.6 and 1.8 $M_\odot$, respectively ('Spectral energy distribution' in Methods). Then the duration of eclipse events would be given by the mutual velocities of the dust clouds and the G subgiant. The eclipses with relatively high observed velocities of up to 90 km s⁻¹ would exclude long-period binaries with slow orbital motions. Note that the centre of mass is close to the G subgiant and that the orbital velocity of the central star of the planetary nebula is about 3× faster than that of the G subgiant. Circumbinary clouds cannot move faster than the velocity of the central star of the planetary nebula, which means that the orbital velocities of the G subgiant and dust clouds cannot be less than about 22 and 66 km s⁻¹, respectively (to sum up to 90 km s⁻¹). Consequently, to explain the shortest eclipses in a circumbinary scenario, the binary separation and the orbital period cannot be larger than about 0.3 au and 30 days, respectively. This does not include the dynamical effects of the binary, which would clean its neighbourhood and push the dust and small bodies farther out with lower orbital velocities, which would require an even more compact binary. However, such binaries are disfavoured by the size of the subgiant, the absence of the reflection effect ('TESS photometry'), the ellipsoidal variability, the spherical shape of the planetary nebula and mainly by the expected luminosity of the central star of the planetary nebula, which would move around the centre of mass and quickly evaporate the dust in its vicinity. For example, assuming an average luminosity of the central star of the planetary nebula of 60 $L_\odot$ (based on evolutionary models; 'Spectral energy distribution' in Methods), the snow line of refractory dust would be at about 0.3 au from the central star of the planetary nebula.

To search for periodicity in the photometric data, we combined together Gaia, ZTF and ASAS data in all filters. First. we subtracted the median value from each dataset and then we merged them together. The variability of the source in the visual region is dominated by the eclipses, and these are almost grey. Hence, combining these data is justified. Then we calculated the Lomb–Scargle periodogram using Peranso[80] covering the interval MJD 56,500–60,000, which is displayed in Supplementary Fig. 2. For comparison, we present the periodogram from the ASAS data alone for the same interval. The ASAS data have the lowest precision, and many measurements within deep eclipses were only upper limits and these were not considered. False alarm probabilities of 1% are indicated in the picture. In such cases, they are not very useful, as most of the frequencies are necessary to compose the observed light curve. The two most important peaks are at 390 and 260 days, and they seem to be in a 2:3 resonance.

Imaging

Narrowband imaging of WeSb 1 was acquired with the Alhambra Faint Object Spectrograph and Camera mounted on the 2.56 m Nordic Optical Telescope (NOT)[81] on the nights of 18 August, 7 October and 14 October 2023. Seven exposures of 750 s were obtained for Hα (NOT filter ID 21, central wavelength λ_{cen} = 656.4 nm and full-width at half-maximum λ_{FWHM} = 3.3 nm) and six exposures of 750 s for [O III] (NOT filter ID 90, λ_{cen} = 500.7 nm and λ_{FWHM} = 3.0 nm). Further narrowband imaging for [O III] (ING filter ID 196, λ_{cen} = 500.8 nm and λ_{FWHM} = 10.0 nm), totalling seven exposures of 1,200 s, was obtained on the nights of 18 and 19 October 2023 using the wide-field camera on the 2.54 m Isaac Newton Telescope (INT).

All the narrowband imaging data were debiased, flat-fielded and cleaned of cosmic rays using the Astropy[82–84] affiliated package ccdproc[85]. The images were then astrometrized using astrometry.net[86] and combined using montage[87].

Images in individual filters are displayed in Supplementary Fig. 3, and a combined false colour image is shown in Fig. 4. The star is clearly visible in both filters with counts more than 100 times above the background. No significant nebular anisotropy was detected in the close vicinity of the central star (3"), which indicates that the shape of the aperture used for spectroscopic observations (described in 'Spectroscopy' in 'Results') did not have a significant impact on the shape of the detected spectral lines. Apart from the properties mentioned in 'Narrowband imaging', the imagery for both narrowband filters shows a bright patch surrounding the central star (seen most clearly in the [O III] filter image) with an angular diameter of roughly 80". It is unclear whether this is a real structure (a bright bubble inside the main nebular shell), due to an illumination effect or a projection effect due to a non-spherical morphology (with the nebula perhaps being bipolar and viewed pole-on). The Hα image does show some signs of wispy filaments that are possibly indicative of low-ionization structures (as seen in, for example, Kn 61; ref. 88).

The proper motion vectors of the star and the stars in its vicinity were taken from ref. 41 and are shown in Fig. 4. To determine the proper motion of the interstellar material (ISM), we considered a cylinder surrounding the location of our star. Its length was twice the uncertainty of the planetary nebula distance, and its radius on the sky was about 5°, which also corresponds to the error in the distance to the star. We considered only stars within the cylinder with precise parallaxes (parallax to error ratio larger than 10). There were 6,757 stars that satisfied those criteria, and their average proper motion vector is (−1.478 ± 0.019, −0.815 ± 0.013) mas yr⁻¹ in right ascension and declination. Taking into account the cosine of the declination, we found the position angle (PA) of the proper motion of the ISM, PA = 226.1 ± 0.6°. This vector is roughly aligned to and of similar size as the proper motion of the star (PA = 209.5 ± 0.5°). Both vectors are also roughly aligned with the axis of symmetry of the nebula and the direction of the central star of the planetary nebula offset from the centre of the planetary nebula, which may not be an accident but probably indicates an interaction between the planetary nebula and the ISM. However, the proper motion vector of the star relative to the ISM points in the other direction (PA = 166.6 ± 1.8°). Because the proper motions of the star and the ISM are very similar, their difference is somewhat small in comparison with the absolute vectors and is very sensitive to the volume of our cylinder. We are bound by the uncertainties in the parallax. Hence, our sample volume is very big (5° radius on the sky). It is possible that local variations in the ISM proper motion inside our cylinder lead to significant changes in the relative proper motion vector. Thus, we warn that our relative proper motion vector may be inconclusive in terms of the interaction of the planetary nebula with the ISM.

The offset of the star from the centre of the planetary nebula is also an open question. Assuming simply that the binary central star ($0.6 + 1.8\,M_\odot$) moves across the sky on a long-period orbit around the common centre of mass with some other unidentified star of a comparable mass ($2.4\,M_\odot$) with a semimajor axis larger than 3" will not work, as it would result in an orbital period of over 10^6 years, which is well above the lifespan of the planetary nebula.

Spectroscopy

We obtained three series of spectra of the star with the 2.56 m NOT on the nights of 15 August, 4 October and 8 December 2023. These dates are indicated by arrows in the bottom panel of Supplementary Fig. 1. The survey photometry indicates that there was little optical variability during these times, with only a 0.6 mag dimming during the third spectrum. There is no significant difference between the spectra. However, the first spectrum is of much better quality, reaching a signal-to-noise ratio in the continuum of about 15. WeSb 1 was observed with the fibre-fed echelle spectrograph (FIES)[89] mounted on NOT[81]. FIES was employed in low-resolution mode (fibre diameter of 2.5") and provided a reciprocal resolution of approximately 25,000 from 3,700–9,000 Å. Three consecutive exposures of 900 s were obtained. These were accompanied by a single 300 s exposure of the standard star BD+28 4211 on 15 August and a single 600 s exposure of the standard star Feige 110 on 4 October[90]. The data were reduced using the FIEStool pipeline. It is important to note that the flux calibration is only approximate given the fibre-fed (and non-sky-subtracted) nature of the observations. Supplementary Table 1 lists the detected spectral lines, their radial velocities and fluxes. Note that, given the apparent brightness of the central star (compared to the extended nebula in the narrowband imaging) and the relative brightness of Hα and [O III] (compared to the stellar continuum in the FIES spectroscopy), the measured emission line fluxes are dominated by a compact, unresolved nebula surrounding the central star rather than the extended background nebulosity.

To constrain the temperature of the hot component, we used the spectroscopic properties of this unresolved nebula. Lines of [Ne III] have the highest ionization potential of about 41 eV. Based on a simple relation between this value and the temperature given by ref. 91, we found a value of about 40 kK. Alternatively, the hydrogen and helium Zanstra temperatures[92,93] of the central star of WeSb 1 could be calculated based on the V magnitude of the central star corrected for nebular emission and extinction ($V_0 = 14.19$). However, as the optical continuum does not correspond to the hot component, we cannot use this Zanstra method. The method of Ambartsumian[94,95] is based on a simple ratio of He II λ4686 and Hβ de-reddened line fluxes. This gives the temperature of the star of about 150 kK, which should be considered as an upper limit. The ratio of [O III] λ5007 plus λ4959 and He II λ4686 line fluxes results in a temperature of about 130 kK, which should be viewed as a lower limit[94]. We warn that these calibrations assume a low-density environment neglecting the collisional excitation. The line ratios λ4363/Hγ and λ5,007/Hβ indicate that our unresolved nebula may be relatively dense in comparison with typical planetary nebulae and these ratios resemble more symbiotic stars[96]. The spectrum of the planetary nebula itself or the UV spectrum of the star would help to put constraints on the temperature of the hot star in the future.

The low signal-to-noise ratio of these high-resolution spectra did not allow us to detect any absorption lines that might be associated with the optical light source (first SED component). Thus, we smoothed the best spectrum with 1- and 2-Å-wide box-shaped filters to boost the signal-to-noise ratio. The result is displayed in Supplementary Fig. 10. For comparison, we show the synthetic spectrum calculated with the code Synspec[97] based on a Kurucz model atmosphere[98] for the effective temperature of 6,000 K, $\log g = 4$ (cgs units), microturbulence of 2 km s^{-1} and solar chemical composition, which was downgraded to the same spectral resolution as the observations. As you can see, we, indeed, detected the absorption lines expected for a star at that temperature, such as Ca, H, Fe and even Ba lines. The observed Ca lines look relatively weak with Ca IIH heavily blended with the Ne and H emission lines. The Ba lines look stronger than expected. Thus, we increased the abundance of Ba by one order of magnitude, which gave a better fit to the data, as also displayed in the figure. What does this mean? It means that the optical source is most probably a G-subgiant companion star. Enhanced Ba lines indicate that the star has been contaminated with material from the central star of the planetary nebula (former AGB donor star).

In connection with the variability of the object in ZTF and ATLAS filters, it is important to know what fraction of energy in these filters is due to nebular emission lines rather than the star. Thus, we performed synthetic photometry on our flux-calibrated spectrum, and then we removed the five strongest emission lines and performed the synthetic photometry again. The magnitudes in ZTF g, ZTF r, ATLAS c and ATLAS o filters increased only by 0.022, 0.013, 0.014 and 0.008 mag, respectively, which translates into the following line/continuum flux ratios: 0.021, 0.012, 0.013 and 0.007, respectively. This indicates that any eclipses deeper than this cannot be caused by variable spectral lines and must, instead, be due to variability or obscuration of the source of the continuum that is the first SED component from 'Spectral energy distribution' in Methods. Moreover, it indicates that these emission lines do not affect the photometric SED considerably.

Photometry

Photometric observations were conducted with the FLI PL-23042 CCD camera mounted in the Nasmyth2 focus of the 1.3 m telescope at Skalnaté Pleso Observatory[99]. This is a $2k \times 2k$ camera with a field of view of 10' × 10' and binning of 2 × 2, which resulted in a pixel scale of about 0.58" per pixel. Its gain was $1.85\,e^-$ per analogue to digital unit, and its read-out noise was $13\,e^-$ (r.m.s.). The star was observed for about 5 h during one night on 15 July 2023. The seeing was about 2" (FWHM). Standard dark and flat-field corrections were done in IRAF followed by aperture photometry with MuniWin 2.0. Four comparison stars with a colour like that of the target were selected and combined into one artificial standard. The resulting differential photometry is shown in Supplementary Fig. 4. The star is almost constant in the R filter (within 0.01 mag), whereas in the B filter, there is weak variability at the level of about ±0.01 mag.

TESS photometry

The TESS mission[47], launched by NASA in 2018, is an all-sky survey providing high-precision time-series photometry. The satellite captures red-optical light across a wide band-pass of approximately 600–1,000 nm, achieving a noise floor of around 60 ppm h^{-1} for optimal targets. TESS provides full-frame images publicly, allowing light curves to be extracted for any sufficiently bright object. TESS observes one field of view 24° × 96° continuously for about 27 days (one sector). At the time of writing, WeSb 1 data are available from TESS sectors 17 and 18 (exposure time 1,426 s during 2019) and from sector 58 (158 s during 2022). Light curves were extracted from TESS. We used the LIGHTKURVE[100] and TESSCUT[101] packages to download a 9 × 9 pixel target pixel file centred on the target star (Supplementary Fig. 11). The detrending was done by background subtraction, such that background pixels were identified in the target pixel file and their average flux level in each frame was subtracted from the target light curve (after accounting for the number of pixels in the adopted aperture).

Unfortunately, the TESS pixel size is very big, about 21". WeSb 1 is relatively faint and in a rather crowded star field, which means that its photometry is contaminated by the stars nearby. For example, a similarly bright but constant object is at a distance of 0.54', which

corresponds to about 1.4 TESS pixels (Gaia DR3 3423384926720604160, Gmag 14.4405). Thus, for our analysis, we used only one central pixel, No. 5, from the full-frame image, which has the highest amplitude for the variability. The light curves are shown in Supplementary Fig. 12. Sectors 17 and 58 contain a few eclipses, and sector 17 was also well covered by ZTF observations, which are shown for comparison. The ZTF data confirm that the variability of this TESS pixel is dominated by the variability of our source. However, the eclipses in the ZTF − r data, which cover a similar spectral region as TESS, are a factor of about 1.4 deeper. This is due to the above-mentioned blending effect. Sector 58 contains five pronounced dips within about 2 weeks. They all look fairly symmetric, which is demonstrated by a fit involving six symmetric Gaussians with a trend as given by equation (4). The symmetry of the events do not favour repeating dust condensation and subsequent dust destruction and dissipation as a driving mechanism of the variability, as the two processes probably have much different timescales. Rather, it supports the eclipsing nature of the events. In fact, it resembles the famous 'string of pearls' (disintegrated comet Shoemaker–Levy 9, which crashed into Jupiter in 1994[102]).

There is no indication of variability that could be associated with the reflection effect or ellipsoidal variations on timescales shorter than 1 month and amplitude larger than about 1% (taking into account the blending effect; see sector 18), which might be expected for a close post-CE binary. One could expect the following relative amplitude for the reflection effect:

$$\frac{\Delta F_\lambda}{F_\lambda} = \frac{[B_\lambda(T_{Gsub}) - B_\lambda(T_G)]R_G^2}{B_\lambda(T_{CSPN})R_{CSPN}^2 + B_\lambda(T_G)R_G^2}, \tag{5}$$

where B_λ is the Planck function. $T_{CSPN} = 100$ kK, $R_{CSPN} = 0.026\,R_\odot$, $T_G = 5{,}890$ K and $R_G = 4.1\,R_\odot$ refer to the effective temperatures and radii of the central star of the planetary nebula and G subgiant, respectively ('Spectral energy distribution' in Methods). Assuming a bolometric albedo of 0.5 (ref. 103), the temperature at the substellar point of the G subgiant would be $T_{Gsub} = 5{,}920$ K. For $\lambda = 7000$ Å and an edge-on binary, these amplitudes are larger than 2% for orbital periods shorter than 15 days. This indicates that our star is probably not such a short-period binary.

Data availability
All of the most relevant photometric data that we used are from the ZTF[44], Gaia[40,41], ASAS-SN[36,37] and TESS[47] projects. The data are publicly available. All proprietary data are available upon reasonable request to the corresponding author.

Code availability
The code that we used to model the SED is an adapted version of the code presented in ref. 58 and can be found at https://github.com/JamesMunday98/WD-BASS.

References
1. Fressin, F. et al. The false positive rate of Kepler and the occurrence of planets. *Astrophys. J.* **766**, 81 (2013).
2. Petigura, E. A., Howard, A. W. & Marcy, G. W. Prevalence of Earth-size planets orbiting Sun-like stars. *Proc. Natl Acad. Sci. USA* **110**, 19273–19278 (2013).
3. Mulders, G. D., Pascucci, I., Apai, D. & Ciesla, F. J. The exoplanet population observation simulator. I. The inner edges of planetary systems. *Astron. J.* **156**, 24 (2018).
4. Matthews, B. C., Krivov, A. V., Wyatt, M. C., Bryden, G. & Eiroa, C. in *Protostars and Planets VI* (eds Beuther, H. et al.) 521–544 (Univ. Arizona Press, 2014).
5. Hughes, A. M., Duchêne, G. & Matthews, B. C. Debris disks: structure, composition, and variability. *Annu. Rev. Astron. Astrophys.* **56**, 541–591 (2018).
6. Mustill, A. J., Veras, D. & Villaver, E. Long-term evolution of three-planet systems to the post-main sequence and beyond. *Mon. Not. R. Astron. Soc.* **437**, 1404–1419 (2014).
7. Stephan, A. P., Naoz, S. & Gaudi, B. S. Giant planets, tiny stars: producing short-period planets around white dwarfs with the eccentric Kozai-Lidov mechanism. *Astrophys. J.* **922**, 4 (2021).
8. Debes, J. H. & Sigurdsson, S. Are there unstable planetary systems around white dwarfs? *Astrophys. J.* **572**, 556–565 (2002).
9. Jura, M. A tidally disrupted asteroid around the white dwarf G29-38. *Astrophys. J. Lett.* **584**, L91–L94 (2003).
10. Vanderburg, A. et al. A disintegrating minor planet transiting a white dwarf. *Nature* **526**, 546–549 (2015).
11. Manser, C. J. et al. A planetesimal orbiting within the debris disc around a white dwarf star. *Science* **364**, 66–69 (2019).
12. Gänsicke, B. T. et al. Accretion of a giant planet onto a white dwarf star. *Nature* **576**, 61–64 (2019).
13. Vanderbosch, Z. et al. A white dwarf with transiting circumstellar material far outside the Roche limit. *Astrophys. J.* **897**, 171 (2020).
14. Vanderburg, A. et al. A giant planet candidate transiting a white dwarf. *Nature* **585**, 363–367 (2020).
15. Blackman, J. W. et al. A Jovian analogue orbiting a white dwarf star. *Nature* **598**, 272–275 (2021).
16. Guidry, J. A. et al. I spy transits and pulsations: empirical variability in white dwarfs using Gaia and the Zwicky Transient Facility. *Astrophys. J.* **912**, 125 (2021).
17. Veras, D. in *Oxford Research Encyclopedia of Planetary Science*, Vol. 1 (ed. Read, P.) (Oxford Univ. Press, 2021).
18. Jones, D. & Boffin, H. M. J. Binary stars as the key to understanding planetary nebulae. *Nat. Astron.* **1**, 0117 (2017).
19. Kluska, J. et al. A population of transition disks around evolved stars: fingerprints of planets. Catalog of disks surrounding Galactic post-AGB binaries. *Astron. Astrophys.* **658**, A36 (2022).
20. Mauron, N. & Huggins, P. J. Imaging the circumstellar envelopes of AGB stars. *Astron. Astrophys.* **452**, 257–268 (2006).
21. Maercker, M. et al. Unexpectedly large mass loss during the thermal pulse cycle of the red giant star R Sculptoris. *Nature* **490**, 232–234 (2012).
22. Perets, H. B. Planets in evolved binary systems. *AIP Conf. Proc.* **1331**, 56–75 (2011).
23. Zorotovic, M. & Schreiber, M. R. Origin of apparent period variations in eclipsing post-common-envelope binaries. *Astron. Astrophys.* **549**, A95 (2013).
24. Guzman-Ramirez, L., Lagadec, E., Jones, D., Zijlstra, A. A. & Gesicki, K. PAH formation in O-rich planetary nebulae. *Mon. Not. R. Astron. Soc.* **441**, 364–377 (2014).
25. Völschow, M., Banerjee, R. & Hessman, F. V. Second generation planet formation in NN Serpentis? *Astron. Astrophys.* **562**, A19 (2014).
26. Schleicher, D. R. G. & Dreizler, S. Planet formation from the ejecta of common envelopes. *Astron. Astrophys.* **563**, A61 (2014).
27. Nixon, C. J., King, A. R. & Pringle, J. E. The maximum mass solar nebula and the early formation of planets. *Mon. Not. R. Astron. Soc.* **477**, 3273–3278 (2018).
28. Rattanamala, R. et al. Eclipse timing variations in the WD + dM eclipsing binary RR Cae. *Mon. Not. R. Astron. Soc.* **523**, 5086–5108 (2023).
29. Esmer, E. M., Baştürk, Ö., Selam, S. O. & Aliş, S. Detection of two additional circumbinary planets around Kepler-451. *Mon. Not. R. Astron. Soc.* **511**, 5207–5216 (2022).
30. Song, S. et al. An updated model for circumbinary planets orbiting the sdB binary NY Virginis. *Astron. J.* **157**, 184 (2019).
31. Bear, E. & Soker, N. First- versus second-generation planet formation in post-common envelope binary (PCEB) planetary systems. *Mon. Not. R. Astron. Soc.* **444**, 1698–1704 (2014).

32. Bilíková, J., Chu, Y.-H., Gruendl, R. A., Su, K. Y. L. & De Marco, O. Spitzer search for dust disks around central stars of planetary nebulae. *Astrophys. J. Suppl. Ser.* **200**, 3 (2012).

33. Marshall, J. P. et al. Evidence for the disruption of a planetary system during the formation of the Helix nebula. *Astron. J.* **165**, 22 (2023).

34. Chornay, N. & Walton, N. A. *VizieR Online Data Catalog: Central stars of planetary nebulae in Gaia DR2 (Chornay+, 2020)* (VizieR, 2020).

35. Miszalski, B., Mikołajewska, J. & Udalski, A. Symbiotic stars and other Hα emission-line stars towards the Galactic bulge. *Mon. Not. R. Astron. Soc.* **432**, 3186–3217 (2013).

36. Shappee, B. J. et al. The man behind the curtain: X-rays drive the UV through NIR variability in the 2013 active galactic nucleus outburst in NGC 2617. *Astrophys. J.* **788**, 48 (2014).

37. Christy, C. T. et al. The ASAS-SN catalogue of variable stars X: discovery of 116,000 new variable stars using G-band photometry. *Mon. Not. R. Astron. Soc.* **519**, 5271–5287 (2023).

38. Law, N. M. et al. The Palomar Transient Factory: system overview, performance, and first results. *Publ. Astron. Soc. Pac.* **121**, 1395 (2009).

39. Butters, O. W. et al. The first WASP public data release. *Astron. Astrophys.* **520**, L10 (2010).

40. Gaia Collaboration. The Gaia mission. *Astron. Astrophys.* **595**, A1 (2016).

41. Gaia Collaboration. Gaia Data Release 3: Summary of the content and survey properties. *Astron. Astrophys.* https://doi.org/10.1051/0004-6361/202243940 (2023).

42. Tonry, J. L. et al. ATLAS: A High-cadence All-sky Survey System. *Publ. Astron. Soc. Pac.* **130**, 064505 (2018).

43. Heinze, A. N. et al. A first catalog of variable stars measured by the Asteroid Terrestrial-impact Last Alert System (ATLAS). *Astron. J.* **156**, 241 (2018).

44. Bellm, E. C. et al. The Zwicky Transient Facility: system overview, performance, and first results. *Publ. Astron. Soc. Pac.* **131**, 018002 (2019).

45. Wright, E. L. et al. The Wide-field Infrared Survey Explorer (WISE): mission description and initial on-orbit performance. *Astron. J.* **140**, 1868–1881 (2010).

46. Mainzer, A. et al. Preliminary results from NEOWISE: an enhancement to the Wide-field Infrared Survey Explorer for Solar System science. *Astrophys. J.* **731**, 53 (2011).

47. Ricker, G. R. et al. Transiting Exoplanet Survey Satellite (TESS). *J. Astron. Telesc. Instrum. Syst.* **1**, 014003 (2015).

48. Miller Bertolami, M. M. New models for the evolution of post-asymptotic giant branch stars and central stars of planetary nebulae. *Astron. Astrophys.* **588**, A25 (2016).

49. Soker, N., Rappaport, S. & Harpaz, A. Eccentric binary model for off-center planetary nebula nuclei. *Astrophys. J.* **496**, 842–848 (1998).

50. Jones, D. et al. Abell 41: shaping of a planetary nebula by a binary central star. *Mon. Not. R. Astron. Soc.* **408**, 2312–2318 (2010).

51. Wareing, C. J., Zijlstra, A. A. & O'Brien, T. J. The interaction of planetary nebulae and their asymptotic giant branch progenitors with the interstellar medium. *Mon. Not. R. Astron. Soc.* **382**, 1233–1245 (2007).

52. Fragkou, V. et al. The planetary nebula in the 500 Myr old open cluster M37. *Astrophys. J. Lett.* **935**, L35 (2022).

53. Bond, H. E. et al. The nucleus of the planetary nebula EGB 6 as a post-Mira binary. *Astrophys. J.* **826**, 139 (2016).

54. Krtička, J., Kubát, J. & Krtičková, I. Stellar wind models of central stars of planetary nebulae. *Astron. Astrophys.* **635**, A173 (2020).

55. Bayo, A. et al. VOSA: virtual observatory SED analyzer. An application to the Collinder 69 open cluster. *Astron. Astrophys.* **492**, 277–287 (2008).

56. Bailer-Jones, C. A. L., Rybizki, J., Fouesneau, M., Demleitner, M. & Andrae, R. Estimating distances from parallaxes. V. Geometric and photogeometric distances to 1.47 billion stars in Gaia Early Data Release 3. *Astron. J.* **161**, 147 (2021).

57. Green, G. M., Schlafly, E., Zucker, C., Speagle, J. S. & Finkbeiner, D. A 3D dust map based on Gaia, Pan-STARRS 1, and 2MASS. *Astrophys. J.* **887**, 93 (2019).

58. Munday, J. et al. The DBL Survey I: discovery of 34 double-lined double white dwarf binaries. *Mon. Not. R. Astron. Soc.* **532**, 2534–2556 (2024).

59. Foreman-Mackey, D., Hogg, D. W., Lang, D. & Goodman, J. emcee: The MCMC hammer. *Publ. Astron. Soc. Pac.* **125**, 306 (2013).

60. Gordon, K. D. et al. One relation for all wavelengths: the far-ultraviolet to mid-infrared Milky Way spectroscopic *R*(V)-dependent dust extinction relationship. *Astrophys. J.* **950**, 86 (2023).

61. Lejeune, T. & Schaerer, D. Database of Geneva stellar evolution tracks and isochrones for (UBV)$_J$(RI)$_C$ JHKLL'M, HST-WFPC2, Geneva and Washington photometric systems. *Astron. Astrophys.* **366**, 538–546 (2001).

62. Budaj, J., Kocifaj, M., Salmeron, R. & Hubeny, I. Tables of phase functions, opacities, albedos, equilibrium temperatures, and radiative accelerations of dust grains in exoplanets. *Mon. Not. R. Astron. Soc.* **454**, 2–27 (2015).

63. Deirmendjian, D. Scattering and polarization properties of water clouds and hazes in the visible and infrared. *Appl. Opt.* **3**, 187 (1964).

64. Alonso, R., Rappaport, S., Deeg, H. J. & Palle, E. Gray transits of WD 1145+017 over the visible band. *Astron. Astrophys.* **589**, L6 (2016).

65. Izquierdo, P. et al. Fast spectrophotometry of WD 1145+017. *Mon. Not. R. Astron. Soc.* **481**, 703–714 (2018).

66. Zhou, G. et al. Simultaneous infrared and optical observations of the transiting debris cloud around WD 1145+017. *Mon. Not. R. Astron. Soc.* **463**, 4422–4432 (2016).

67. Xu, S. et al. A dearth of small particles in the transiting material around the white dwarf WD 1145+017. *Mon. Not. R. Astron. Soc.* **474**, 4795–4809 (2018).

68. Croll, B. et al. Multiwavelength transit observations of the candidate disintegrating planetesimals orbiting WD 1145+017. *Astrophys. J.* **836**, 82 (2017).

69. Hallakoun, N. et al. Once in a blue moon: detection of 'bluing' during debris transits in the white dwarf WD 1145+017. *Mon. Not. R. Astron. Soc.* **469**, 3213–3224 (2017).

70. Xu, S. et al. Shallow ultraviolet transits of WD 1145+017. *Astron. J.* **157**, 255 (2019).

71. Budaj, J., Maliuk, A. & Hubeny, I. WD 1145+017: alternative models of the atmosphere, dust clouds, and gas rings. *Astron. Astrophys.* **660**, A72 (2022).

72. Weinberger, R. & Sabbadin, F. Detection of six new extended planetary nebulae by means of interference filter photography. *Astron. Astrophys.* **100**, 66–67 (1981).

73. Rosado, M. & Moreno, M. A. Deep narrow band interference filter photographs of selected extended planetary nebulae. *Astron. Astrophys. Suppl. Ser.* **88**, 245 (1991).

74. Kohoutek, L. Version 2000 of the Catalogue of Galactic Planetary Nebulae. *Astron. Astrophys.* **378**, 843–846 (2001).

75. Chornay, N. & Walton, N. A. *VizieR Online Data Catalog: Gaia EDR3 planetary nebula central star distances (Chornay+ 2021)* (VizieR, 2021).

76. Bojičić, I. S., Parker, Q. A. & Frew, D. J. The Hong Kong/AAO/Strasbourg Hα (HASH) Planetary Nebula Database. In *Proc. International Astronomical Union, Volume 12, Symposium S323: Planetary Nebulae: Multi-Wavelength Probes of Stellar and Galactic Evolution*, Vol. 12 (eds Liu, X. et al.) 327–328 (Cambridge Univ. Press, 2017).

77. Frew, D. J., Parker, Q. A. & Bojičić, I. S. The Hα surface brightness-radius relation: a robust statistical distance indicator for planetary nebulae. *Mon. Not. R. Astron. Soc.* **455**, 1459–1488 (2016).

78. Jayasinghe, T. et al. The ASAS-SN catalogue of variable stars I: The Serendipitous Survey. *Mon. Not. R. Astron. Soc.* **477**, 3145–3163 (2018).

79. Kennedy, G. M. et al. The transiting dust clumps in the evolved disc of the Sun-like UXor RZ Psc. *R. Soc. Open Sci.* **4**, 160652 (2017).

80. Paunzen, E. & Vanmunster, T. Peranso—Light curve and period analysis software. *Astron. Nachrichten* **337**, 239 (2016).

81. Djupvik, A. A. & Andersen, J. in *Highlights of Spanish Astrophysics V* (eds Diego, J. M. et al.) 211 (2010).

82. Astropy Collaboration. Astropy: a community Python package for astronomy. *Astron. Astrophys.* **558**, A33 (2013).

83. Astropy Collaboration. The Astropy Project: building an open-science project and status of the v2.0 core package. *Astron. J.* **156**, 123 (2018).

84. Astropy Collaboration. The Astropy Project: sustaining and growing a community-oriented open-source project and the latest major release (v5.0) of the core package. *Astrophys. J.* **935**, 167 (2022).

85. Craig, M. et al. astropy/ccdproc: 2.4.1. *Zenodo* https://doi.org/10.5281/zenodo.7986923 (2023).

86. Lang, D., Hogg, D. W., Mierle, K., Blanton, M. & Roweis, S. Astrometry.net: blind astrometric calibration of arbitrary astronomical images. *Astron. J.* **139**, 1782–1800 (2010).

87. Jacob, J. C. et al. Montage: an astronomical image mosaicking toolkit. *Astrophysics Source Code Library* ascl:1010.036 (2010).

88. García-Díaz, M. T. et al. A spectroscopic and photometric study of the planetary nebulae Kn 61 and Pa 5. *Astron. J.* **148**, 57 (2014).

89. Telting, J. H. et al. FIES: the high-resolution fiber-fed echelle spectrograph at the Nordic Optical Telescope. *Astron. Nachrichten* **335**, 41 (2014).

90. Stone, R. P. S. Spectral energy distributions of standard stars of intermediate brightness. II. *Astrophys. J.* **218**, 767–769 (1977).

91. Murset, U. & Nussbaumer, H. Temperatures and luminosities of symbiotic novae. *Astron. Astrophys.* **282**, 586–604 (1994).

92. Zanstra, H. Temperatures of stars in planetary nebulæ. *Nature* **121**, 790–791 (1928).

93. Pottasch, S. R. *Planetary Nebulae. A Study of Late Stages of Stellar Evolution*, Vol. 107 (Springer, 1984).

94. Gurzadyan, G. A. *The Physics and Dynamics of Planetary Nebulae* (Springer, 1997).

95. Skopal, A. et al. New outburst of the symbiotic nova AG Pegasi after 165 yr. *Astron. Astrophys.* **604**, A48 (2017).

96. Iłkiewicz, K. & Mikołajewska, J. Distinguishing between symbiotic stars and planetary nebulae. *Astron. Astrophys.* **606**, A110 (2017).

97. Hubeny, I., Allende Prieto, C., Osorio, Y. & Lanz, T. TLUSTY and SYNSPEC Users's Guide IV: Upgraded Versions 208 and 54. Preprint at https://arxiv.org/abs/2104.02829 (2021).

98. Castelli, F. & Kurucz, R. L. New grids of ATLAS9 model atmospheres. Preprint at https://arxiv.org/abs/astro-ph/0405087 (2004).

99. Pribulla, T. et al. Affordable échelle spectroscopy with a 60 cm telescope. *Astron. Nachrichten* **336**, 682 (2015).

100. Lightkurve Collaboration. Lightkurve: Kepler and TESS time series analysis in Python. *Astrophysics Source Code Library* ascl:1812.013 (2018).

101. Brasseur, C. E., Phillip, C., Fleming, S. W., Mullally, S. E. & White, R. L. Astrocut: tools for creating cutouts of TESS images. *Astrophysics Source Code Library* ascl:1905.007 (2019).

102. Weaver, H. A. et al. The Hubble Space Telescope (HST) observing campaign on comet Shoemaker–Levy 9. *Science* **267**, 1282–1288 (1995).

103. Ruciński, S. M. The proximity effects in close binary systems. II. The bolometric reflection effect for stars with deep convective envelopes. *Acta. Astron.* **19**, 245 (1969).

Author contributions

Competing interests

The authors declare no competing interests.

Additional information